FEASIBILITY OF ACTIVE DEBRIS MITIGATION USING SPACE-BORNE LASERS

L. Walker and M. Vasile

University of Strathclyde, James Weir Building, 75 montrose Street, Glasgow, United Kingdom, G1 1XJ Email: {lewis.walker, massimiliano.vasile}@strath.ac.uk

ABSTRACT

Small (<10cm) debris fragments present a significant threat to all operational satellites in orbit. Although numerous strategies for debris mitigation have been proposed, most active space-based methods involve rendezvous maneuvers with targeted pieces of debris, making them unsuitable for the cleaning up of large populations of fragments. There are more appropriate for removing larger objects which are potential sources of further debris. Moreover, these types of strategies are inapplicable to fragments which are too small to be tracked from Earth to facilitate rendezvous. To date few strategies have been proposed to deal with large numbers of fragments, particularly as a response to collision events, which is the focus of this paper.

This paper investigates through numerical simulations the impact of an active debris mitigation strategy using space-based lasers, targeted at debris shells resulting from collision events. A concept is proposed that allows for opportunistic interaction with debris, without rendezvous, with zero knowledge of individual fragments' orbits from ground-based observations. The impact of the mission is simulated numerically by analyzing the dynamics of typical encounters and employing high-fidelity models of both photon pressure and laser ablation based interaction mechanisms.

The goal of this example mission concept is to reduce the average lifetime of a debris cloud, rather than completely deorbiting individual fragments. This work builds on previous work by Vasile et. al. who proposed a similar concept in 2011.

Keywords: Space Debris; Photon Pressure; Laser Ablation; Satellite Constellations.

1. INTRODUCTION

With space launch costs decreasing due to the advent of reusable rockets and cheap dedicated smallsat launch vehicles, the number of satellites in Earth orbit will increase significantly over the coming years and decades as space becomes accessible to smaller institutions and private for-profit ventures. The first private megaconstellations are already being deployed for global low-latency satellite internet access. As the number of satellites grows and expand to higher orbits, the risk of collisions and collision chains (the so-called Kessler syndrome) increases also, and so debris mitigation strategies must be developed to prepare for eventual collision events.

Satellite collision events, for example the 2009 Iridium-Kosmos collision, or deployment of anti-satellite weapons leave behind higher-density orbital regions of debris which will spread out into shells [3] and slowly decay due to small amounts of atmospheric drag. If a new collision event(s) were to occur, the resultant debris shells could render certain orbital altitude bands around the colliding satellites unusable or, at the very least, highly dangerous to pass through until the population naturally deorbits. This is particularly problematic for higher orbits where the atmosphere is more sparse, and hence fragments take longer to decay. Due to the large numbers of fragments produced in such collisions, mitigation strategies involving rendezvous, capture, and deorbiting are impractical because of the fuel cost making these strategies suitable only for the removal of defunct satellites or larger fragments which represent potential sources of further debris.

Several strategies have been proposed to remove larger objects such as defunct satellites. These generally involve rendezvous and mechanical interaction such as harpoons or nets, before using the spacecraft's engine to deorbit the object. However, as mentioned these strategies involving rendezvous are impractical for dealing with large numbers of small fragments due to huge propellant expenditure.

Proposed laser-based strategies employing photon pressure have been primarily ground-based, with the intention being collision avoidance over removal. These concepts, such as LightForce [**?**], employ one or several ground-based continuous-wave (CW) lasers which illuminate the target fragment with each pass overhead. These strategies require that the fragments are trackable from Earth and that their orbits be known in advance of interactions.

As for ablation based strategies, L'ADROIT [5] is the most well-developed, space-based concept, where a sin-

gle large satellite is proposed in an elliptical polar orbit between 560-960 km. However, there are some issues with some assumptions made therein - for example, perfect laser alignment with the debris' negative velocity vector, quickly variable-focussable laser beam with the beam waist plane precisely aligned with the fragments. These two unrealistic assumptions increase the found effectiveness of the intervention. Additionally, the targeted altitude band, as will be discussed in this paper, already has a relatively short orbital lifetime, making the potential return on investment limited. The concept proposed in this paper is similar to L'ADROIT, with key differences being that many, smaller satellites are used, and the targeted orbit is higher. The dynamics of interactions here are also simulated more accurately, removing some optimizing assumptions.

Space-based platforms have several advantages over ground-based versions. These are primarily due to the lack of atmospheric scattering, shorter range to target (resulting in higher fluence at target) particularly at higher orbits, and improved directionality of the applied force, with the net force vector being closer to the negative velocity direction. It is true however that some disadvantages of ground-based systems could be offset by simply constructing more powerful lasers on the ground, as their size, weight and power restrictions are far more generous.

2. CONCEPT OVERVIEW

2.1. Lifetime Reduction from Small Velocity Changes

Since the net velocity change from laser-based interaction is expected to be small, an initial study on the effect of small orbit adjustments was performed to assess the lifetime impact of small impulsive ΔV applications at varying altitudes. Since lower fragments already deorbit rather quickly, it is expected that more meaningful lifetime reductions could be achieved for higher orbits. However, as the orbit gets higher, the spatial density of debris and the subsequent interaction rate would lower for a roughly uniform shell. Thus this class of mitigation strategy should be targeted at orbits that are high enough to have relatively long lifetimes, while not being so high that the interaction rate becomes very low.

Orbits are propagated in this paper using a tool developed at the University of Strathclyde called CALYPSO. CALYPSO propagates orbits semi-analytically, taking into account perturbations including atmospheric drag, third body and J2-J4 perturbations. However, for the sake of computational efficiency, propagations herein are performed with drag as the only perturbation. For modelling atmospheric drag, the volume, size and area-to-mass ratio (AMR) of a 3D model of a 2cm aluminium hex nut to represent debris fragments. The AMR of this 3D model is 0.3391. This coincides approximately with the peak of the distribution of the catalogued debris from the Iridium-Cosmos collision [10].

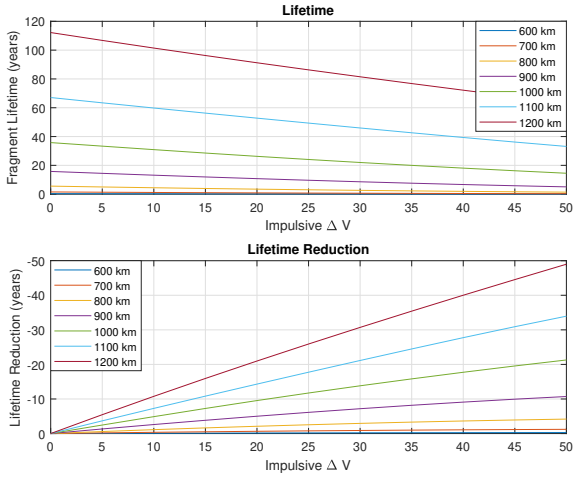

Figure 1. Lifetime and lifetime reduction with an impulsive ΔV for circular, 45 degree inclined orbits of varying altitude

Circular orbits of varying altitudes, inclined at 45 degrees were propagated until reentry. An initial impulsive ΔV was applied in the negative velocity direction ranging from zero to 50 ms^{-1}. The effects on the time-to-reentry can be seen in Figure 1.

It can be seen that, for higher orbits, a given ΔV application results in a larger absolute lifetime reduction, as expected. For lower orbits, the reduction becomes less meaningful - for example for 700 km altitude, the expected lifetime is already under 10 years, so smaller ΔV interventions may only reduce a fragment's life by a couple of months at best. Whereas for a 1200km orbit, smaller ΔV has a more significant impact, with only 10 ms^{-1} reducing lifespan by over 10 years.

Taking this into account, for the remained of this paper we consider a case of 1200km, 45 degree inclined orbits as the basis for feasibility assessment.

3. DEBRIS SHELL CHARACTERISTICS

A debris population representative of that produced by a collision event must be generated for this analysis. TLE data (obtained November 2020) is available for the tracked fragments from the 2009 Iridium-Cosmos collision, which can be compared with the pre-collision orbits of the two satellites to assess how the cloud characteristics compare with the orbit of the satellites.

It was found that the altitude and inclination followed approximately normal distributions, close to the pre-collision values of the satellties. Inclination was very tightly clustered around the pre-collision value, with stan-

dard deviations of 0.051^o for the Iridium-33 cloud and 0.0326^o for the Kosmos-2251 cloud. Altitude was found to have dissipated more over time due to differential drag effects, with standard deviation of 76.4 km and 79.0 km. The eccentricity distribution can be approximated by a log-normal distribution, with no discernable link between the satellite eccentricity and the curve parameters. The right ascension of the ascending node and true anomaly had both dispersed to a quasi-uniform distribution, as expected from [3].

For the modelling in this paper, a debris population was generated to simulate that which might be produced by the breakup of a satellite in a 1200 km, circular orbit, inclined at 45 degrees, based on these distributions. Altitude and inclination were generated with a normal distribution with standard deviation equal to the average of the standard deviations of the Iridium-Cosmos cloud distributions. Eccentricity was generated using a log-normal distribution with parameters equal to the average of those of the Iridium-Cosmos distributions, as both satellites were in near-circular orbits before the collision. The other orbital elements were generated as uniform random numbers between 0 and 359.9 degrees.

4. ENCOUNTER DYNAMICS

In order to determine the long-term impact of the concept, a quasi-statistical approach must be used due to the computational demand of propagating thousands of fragments and computing their interactions with the spacecraft. To achieve this, a small, representative population of 632 fragments is propagated over a 10-year mission span, as well as the orbit of a single satellite. The slowly-changing equinoctal elements can then be interpolated for any instant of interest in the span, and converted to Cartesian to allow analysis of the encounter dynamics to be performed.

The separation between the spacecraft and a given fragment oscillates, producing many local minima over the span. To improve efficiency, local minima are first identified approximately with a 10-second timestep, before being refined to the nearest half-second.

These precise separation local minima, which we shall call 'approach events', are saved along with the states of the spacecraft and fragment at the instant of closest approach, in order to apply conditions in a decision tree to determine if camera acquisition - and subsequently laser interaction - may be possible in each event.

The first downselection is performed by setting a geometric requirement on the configuration at the moment of closest approach. If the vector going from the spacecraft to the fragment is called $\mathbf{S}$, and $\mathbf{V}_{sc}$ is the velocity vector of the spacecraft at the moment of closest approach, then the angle between $\mathbf{S}$ and -$\mathbf{V}_{sc}$ must be less than 30 degrees. This firstly ensures that the fragment is behind the spacecraft during the interaction. Since the orbit of the fragment is not known, a condition on its orbit cannot be used, however ensuring that the fragment is behind the spacecraft increases likelihood that net force will have a significant along-track component acting to lower its orbit. This is because, if the fragment is moving slowly enough across the field of view to be successfully imaged, the orbits must be similar. It also accounts for the limited field of view of the camera, which is modelled as 30 degrees in the simulations in this paper. With multiple cameras, or a sky-scanning pattern, plus or minus one full FoV can be imaged relative to the direction -$\mathbf{V}_{sc}$. If this cannot be achieved practically, plus or minus one half FoV should be used.

The second condition relates to detectability by the camera system and determining if sufficient signal to noise ratio (SNR) is achievable for a given event. For any given noise condition, the exposure duration can always be increased until the required SNR is achieved, in absence of pixel saturation. However, if there is relative motion between the object and the camera and tracking is not possible, the object will move across the field of view. The condition for detectability then becomes that the required SNR must be achievable *before* the object moves to the next pixel.

The relative angular velocity of the downselected events is now calculated. Let $\underline{S}$ be the separation vector originating at the spacecraft and ending at the fragment. Let $\underline{V_R}$ be the velocity of the fragment relative to the satellite. $\underline{V_R}$ has a component perpendicular to $\underline{S}$, which we shall call $\underline{V_P}$, where $\underline{V_P} = \sin(\phi)\underline{V_R}$, where ϕ is the angle between $\underline{S}$ and $\underline{V_R}$. At the instant of closest approach - where the relative angular velocity will be highest - the angular velocity can be found geometrically (Equation 1).

$$\frac{d\theta}{dt} = \frac{\sin(\phi)\underline{V_R}}{\underline{S}} \tag{1}$$

4.1. Optical Acquisition

Analysis on optical acquisition is performed by estimating the SNR of pixels containing the fragment compared with background pixels. SNR is here defined as the ratio of the mean signal photon count on a pixel containing the fragment (μ_s), to the standard deviation of the noise counts in background pixels (σ_n) (Equation 2.

$$SNR = \frac{\mu_s}{\sigma_n} = \frac{\mu_s}{\sqrt{\mu_n}} \tag{2}$$

The expected, or mean, signal photon count per pixel per exposure, μ_s, can be derived from first principles and written as

$$\mu_s = \frac{\Phi_\odot \Delta\lambda A_F \alpha_F \lambda A_{col} \eta_c}{2\pi R^2 hc n_{px}} t_{exp} \tag{3}$$

Where $\Phi_\odot$ is the solar irradiance in $Wm^{-2}nm^{-2}$, $\Delta\lambda$ is the bandwidth of the camera, A_F is the illuminated surface area of the fragment visible to the spacecraft, α_F is the albedo of the fragment in the chosen wavelength band, λ is the central wavelength of the CCD's sensitive band, R is the distance to the fragment, h is Planck's constant, A_{col} is the area of the light collecting optic, η_c is the overall photon-to-electron conversion efficiency of the entire camera-CCD system, t_{exp} is the exposure duration, and $n_{px,i}$ is the number of pixels that the object's image is spread across, which is the point spread function (PSF) for sub-pixel sized sources as will be the case in this scenario.

Background, or noise, counts in a CCD typically consist of several sources - dark counts, non-image photons in the field of view, and readout noise. In this case, we assume negligible non-image photons, as observations will not be made while the Sun is in the field of view, the aperture would have a sun-blocking baffle, and the camera will be kept pointed above the horizon, with the Earth also outside of the field of view. Thus the noise is dominated by dark noise and readout noise. The mean noise photon count *per pixel* can be written as

$$\mu_n = Dt_{exp} + R \tag{4}$$

Where D is the mean dark count rate per pixel, and R is the mean readout noise per pixel per exposure. In space-based CCD imagers, sub-100 Hz/px dark count rates have been demonstrated with active cooling, with around 10 Hz/px being achievable at temperatures of -30 Celsius [2]. Given the large capacity power delivery and storage systems that will be required for the laser system on board each satellite for this mission, it is reasonable to assume CCD active cooling will be available to reduce dark count rate to the 10 Hz/px level, so this is the level used in the base case calculations.

As mentioned previously, the maximum exposure is limited by the angular velocity of the fragment as it moves across the field of view onto adjacent pixels. It is thus important to account for this in the analysis of encounter dynamics. A binary number indicating if the two conditions are fulfilled at a given time instant can be calculated by comparing the relative angular velocity at a given instant in the encounter with the minimum required exposure for a given SNR. An example of this can be seen in Figure 4.1, with the orange line indicating when the conditions are fulfilled.

Figure 3 shows the minimum required exposure for SNR 3, 5, and 10 as a function of distance from the fragment, using the parameters in Table 1, which are the assumed camera parameters for this analysis.

Using the above data, it is possible to determine if a fragment is observable at a specific point in any encounter event.

The illuminated area chosen in these calculations was

Parameter	Value
Circular Aperture Diameter	20 cm
Fragment Albedo	0.5
Camera Efficiency	40%
Bandwidth	350 nm
Solar Irradiance	1.5 $\mathrm{Wm^{-2}nm^{-1}}$
Debris Illuminated Area	2.034e-4 $\mathrm{m^2}$
PSF	4 pixels
Central Wavelength	550 nm
Exposure Duration	0.1339 seconds
Dark Count Rate	10 hz $\mathrm{px^{-1}}$
Mean Read Noise	5 counts $\mathrm{exposure^{-1}}$ $\mathrm{px^{-1}}$

Table 1. Parameters used in imaging SNR analysis

was that of the 3D model of the hex nut, along the direction of the axis passing through the central hole.

From the analyses in this section it is also possible to extract information on the rate of interaction. Timestamps of all viable interactions were used to obtain the distribution of the time between consecutive events. The mean time between events is 41802 seconds, or on average 0.483 encounters per day. When scaling up from the smaller population of 632 fragments to a more realistic population of 5000, the expected event rate is approximately 4 encounters per day. This high encounter rate suggests that the rate of interaction is likely to be limited by the power system and not the encounter dynamics.

5. LASER INTERACTION MODELLING

In order to precisely quantify the force being applied to the fragment, a high fidelity model of photon pressure and ablation over 3D shapes was developed. The model takes a user-defined 3D model of a debris fragment, triangulates the surface and calculates the net laser pressure force and torque vectors at each timestep. In the case of photon pressure, where the interaction occurs over an extended timeframe, this is used to update the velocity and rotation state with each timestep, and incrementally sum the impulse at each timestep, to obtain the net momentum transfer vector over the simulated period. For the ablative mode, interactions are computed in a single instant - these interactions are treated as completely impulsive. In this section we describe the workings of the model.

5.1. Element Illumination

After the 3D model has been triangulated and divided into elements, the illumination state I of each element must be determined to allow force calculation. This effectively modifies the area of the element to account for partial illumination. First, back face culling is applied by setting $I = 0$ for all elements where $\hat{\mathbf{n}} \cdot \hat{\mathbf{i}} > 0$, where $\hat{\mathbf{n}}$ is the element's normal vector and $\hat{\mathbf{i}}$ is the direction of the incident light. Then, occluded vertices are detected by searching

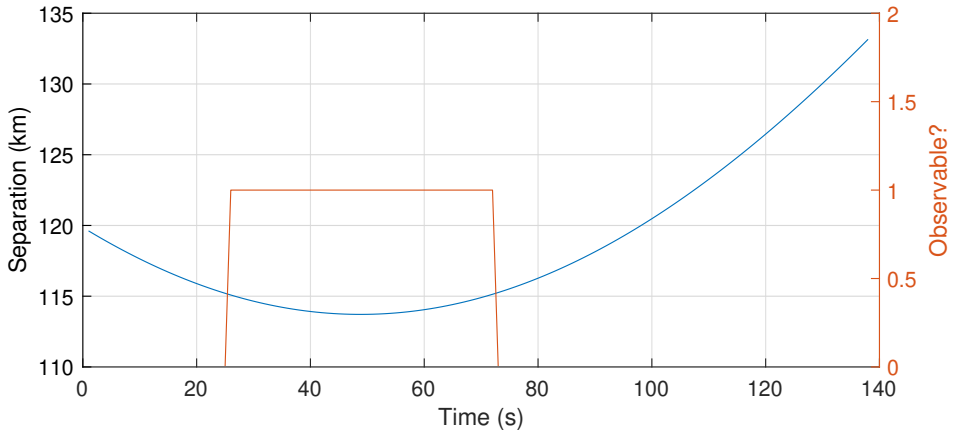

Figure 2. Example of information extracted on the dynamics of a single encounter. The orange curve (right axis) is the binary condition where 1 denotes the fragment is observable at that instant. The full states of both the satellite and fragment are extracted from each encounter.

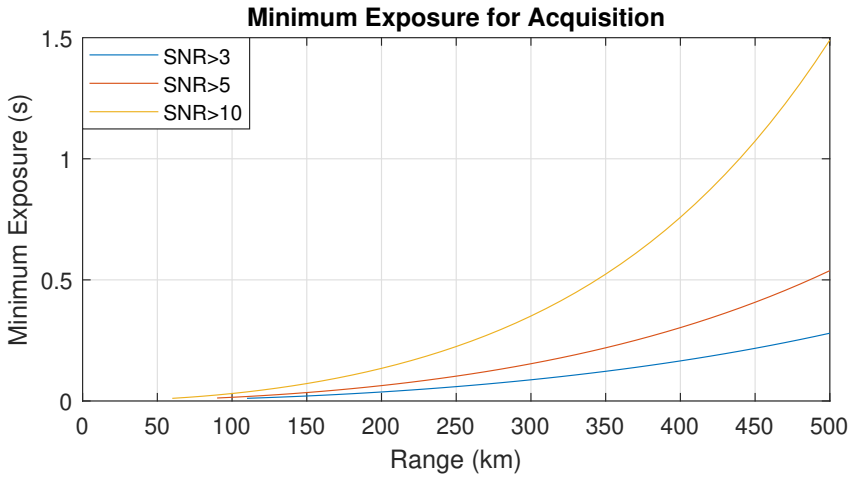

Figure 3. Minimum required exposure at a given range to achieve the specified SNR.

for intersections between other elements and the direction $-\hat{\mathbf{i}}$, originating at the vertex in question. For each element, an illumination state is assigned depending how many of the three vertices are illuminated. For example, if no vertices are illuminated, $I = 0$, and if two are illuminated then $I = \frac{2}{3}$. This illumination state is used as a modifier for the area of a given fragment, to approximate is as one third illuminated, etc.

5.2. Photon Pressure Force

When light is incident on a surface, some fraction is absorbed and the remainder is reflected. The reflected component can be further divided into diffuse and specular components - in diffuse reflection, photons are scattered in all directions due to roughness in the surface. In specular reflection, distinct rays of light reflect from the surface like a mirror, obeying Snell's law. For metallic space debris, the specular component is likely to be non-negligible. In order to accurately calculate the net momentum transfer, all three components should be modelled and their respective force components simulated.

$$\mathbf{F}_e = S\mathbf{F}_{specular} + (1-S)\mathbf{F}_{isotropic} + \mathbf{F}_{absorption} \quad (5)$$

Where S is a specularity factor between 0 and 1 which determines the fraction of light that is reflected specularly. For isotropic diffuse reflection the rate of momentum transfer for each direction of reflected light must simply be integrated over 180 degrees. All transverse components cancel so only the surface-normal components need be integrated. Upon completing this integration, the relation in Equation 6 is obtained.

$$\mathbf{F}_{isotropic} = -\frac{2\alpha P_{laser} I A_s}{\pi c}\hat{\mathbf{n}} \quad (6)$$

where $A_s = A(\hat{\mathbf{n}}\cdot\hat{\mathbf{i}})$ is the area of the surface presented to the direction of the light source, in this case the presented area of each surface element of the triangulated mesh. A is the full area of the element, α is the albedo of the material, $\hat{\mathbf{n}}$ is the unit normal vector of the surface element, P_{laser} is the power per unit area of incident light and c the speed of light.

For the specular component, the net force is equal to

$$\mathbf{F}_{specular} = -\frac{\alpha P_{laser} I A_s}{c}\hat{\mathbf{r}} \quad (7)$$

where $\hat{\mathbf{r}}$ is the unit vector of the direction of the reflected light. The force on the surface element due to absorption is

$$\mathbf{F}_{absorption} = \frac{(1-\alpha) P_{laser} I A_s}{c}\hat{\mathbf{i}} \quad (8)$$

where $\hat{\mathbf{i}}$ is the direction of the incident light.

The algorithm finds the total force for each surface element and the sum to find the net force on the object at each timestep:

$$\mathbf{F}_{net}(t_i) = \sum_{e=1}^{N} \mathbf{F}_e(t_i) \quad (9)$$

where t_i denotes timestep i, N is the total number of elements in the 3D model and $\mathbf{F}_e$ if the net force on element e calculated using Equations 5-8.

Torque is calculated by taking the cross product $\mathbf{F}_e \times \mathbf{R}_e$, where $\mathbf{R}_e$ is the vector connecting each element's center (mean of the vertices) to the object's center of mass.

For propagation to the next timestep, the object's current velocity, angular velocity magnitude and instantaneous axis of rotation are updated from the net force and net torque. The equation for angular velocity update is

$$\omega_i = \omega_{i-1} + \omega_{i-1} dt \quad (10)$$

where τ_i is the net torque vector at timestep i, dt is the timestep size, ω_i is the angular velocity vector at timestep i, and

$$\omega_{i-1} = \frac{\tau_i}{\hat{\mathbf{a}}\mathbf{I}\hat{\mathbf{a}}^T} \quad (11)$$

where

$$\hat{\mathbf{a}} = \frac{\tau_i}{\|\tau_i\|} \quad (12)$$

is the instantaneous axis of angular acceleration, $\mathbf{I}$ is the inertia tensor of the 3D model, and the denominator of Equation 11 is the moment of inertia along the direction $\hat{\mathbf{a}}$.

5.3. Ablation Force

In ablative coupling, an intense pulse of light vaporizes and removes a small amount of material from the surface of the object. The resulting gas and plasma expands and exerts a force on the source material. The strength of the impulse coupling coefficient C_m is approximately 3-4 orders of magnitude higher than that of photon pressure. C_m rises rapidly with the laser fluence, before plasma production begins, shielding the material from further ablation [4]. At this point C_m begins to slowly decline. There exists an optimum fluence Φ_{opt} which maximises C_m, however this is material, wavelength, and

pulse duration dependent [4]. Ablation and impulse coupling coefficients in metals and polymers have been studied experimentally with the main motivation being applications to high specific impulse micro-thrusters and data is available in the literature, however data is somewhat sparse and values take a rather large spread in the available papers. For aluminium, Φ_{opt} has been reported as 11.7 kJm^{-2} at 130fs pulse duration [4], and around 100 kJm^{-2} [11]. As for C_m, there is better agreement between sources, with values ranging from 10 - 30 μJsW^{-1} [4] [11] [6]. A constant value of 20 μJsW^{-1} is used in the simulations in this paper, although if a more robust empirical relationship between C_m and fluence could be obtained, that would allow more accurate modelling of the impulse transfer, since with varying distance in this mission concept, the fluence will vary also. Although a relation between fluence and C_m is not coded into the simulations in this paper, the fluence is still allowed to vary with range as the spot size changes. A pulse energy of 3 kJ was selected which achieves a fluence of approximately 100 kJ/m^2 at the beam waist

For the ablative version of the model, the same illumination detection method is used to apply back-face and collusion culling, then a modifier to the projected area of each fragment. The net ablation force for a given illumination condition is calculated according to Equation 13.

$$\mathbf{F}_{ablation} = C_m \frac{E_{pulse}}{A_{beam}} \sum_i I_i A_{s,i} \hat{\mathbf{n}}_i \qquad (13)$$

where the sum over i is a sum over surface elements, E_{pulse} is the pulse energy and A_{beam} is the area of the beam at the distance in question from the emitter - thus the ratio of the latter two is the fluence. Each element's contribution to the force is assumed to be in the normal direction for that element, since the plume expands in that fashion [1].

5.4. Mass Removal Considerations

During the ablation process, mass must be removed from the target to facilitate the impulse application. However, similarly to the momentum coupling coefficient, mass removal rates are difficult to find in the literature. [9] reported experimental data indicating a mass removal rate on the range of 10^{-9} to 10^{-8} kg/J, and a value of 8x10^{-8} kg/J was used in calculations in an earlier study on a space debris mitigation concept [7]. In low pressure conditions, mass removal rates even less than 10^{-9} kg/J have been reported for aluminium [8]. For comparison, the mass of the hexnut model used in these simulations is 1.2 grams, and the typical total energy imparted on the target in a single pulse is on the order 0.1 - 1 Joule. For a single interaction of 300 pulses, using the higher value of 80 x 10^{-9} kg/J and a total energy incidence of 0.5 J, only 12 mg of material would be ablated, or 1% of the fragment's mass. For the lower value of 10^{-9} kg/J, this becomes 1.5 x 10^{-6} kg mass loss per interaction, or 0.13%.

While these reported figures make it clear that for small-size debris, mass removal is not negligible if there are many pulses, lack of a method for updating the 3D model to account for mass removal meant that this effect had to be neglected. However, it should be noted that if the mass loss rate is on the high end of the range found in literature, it is very likely that small fragments would be completely vaporized before the ablation force would deorbit them. Thus this concept would require alterations to make complete vaporization in a single pass the primary goal. This has been identified by the authors as an area for future study.

5.5. Longitudinal Laser Profile

For a Gaussian, near-single-mode beam, divergence reaches its minimum possible value of $\theta_d = M^2 \frac{\lambda}{2\pi w_0}$, where λ is the laser wavelength and w_0 is the beam waist radius - the radius of the most tightly focussed point along the beam axis. The factor M^2 (greater than or equal to 1), known as the beam quality factor, is added to this expression to capture any deviation from the theoretical minimum, perfectly Gaussian beam profile.

From this, simple geometry allows the beam radius $w(R)$ at any given longitudinal distance from the focal plane (or beam waist) to be calculated according to Equation 14, where R is the distance from the emitter and z_0 is the focal plane's distance from the emitter - thus the term in brackets is the distance of the point of interest from the focal plane. w_0 is the waist radius.

$$w(R) = w_0 + \sqrt{(R - z_0)^2} \tan(\theta_d) \qquad (14)$$

This section will discuss optimizations of the focal plane location and waist radius to increase the irradiance delivered to fragments during interaction.

The simplest approach would be to simply have the waist radius at the emitter, or $z_0 = 0$. However, since this concept deals with long ranges and the effect of the interaction depends heavily on the irradiance of illumination of a fragment, alternatives should be explored that allow for higher irradiance to increase effectiveness and/or reduce laser requirements. Agile, variable-focus optics are not assumed to be available on the spacecraft due to mass and size restrictions.

It is important to note that z_0 cannot be freely chosen, but is constrained by the maximum size of the emitter on board the spacecraft. The required emitter radius can be obtained from Equation 14 by setting $R = -z_0$. Figure 4 shows the relationship between desired waist radius and required emitter size, with z_0 fixed at several values.

It can be seen that larger emitters allow the waist to be placed further away from the craft, and thus a higher fluence to be delivered to the target. A constraint on the size of the emitter must exist since it must fit on board the

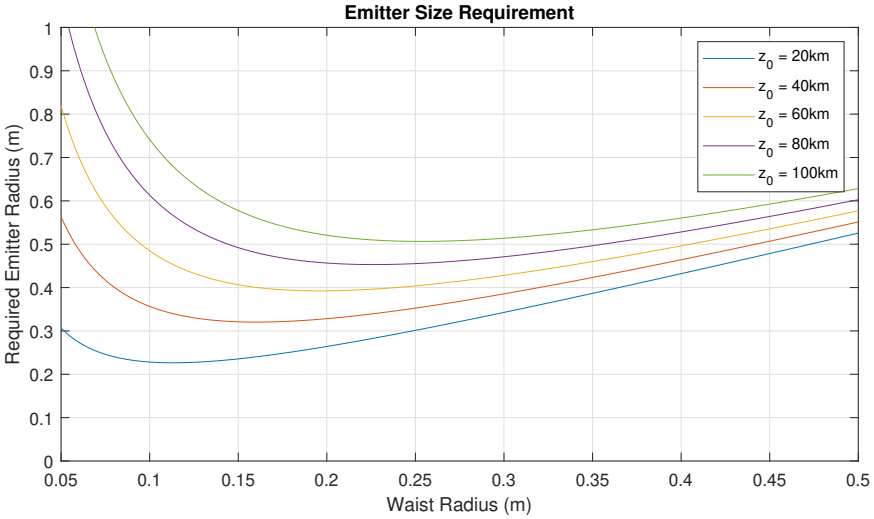

Figure 4. Emitter size requirement for various z_0 and w_0

spacecraft, but precisely defining this is outwith the scope of this paper. An approximate upper limit of $w_e = 0.1$ m was chosen to constrain the parameters z_0 and w_0. Since long distance interactions are required, it is desirable to have the focal plane as far from the spacecraft as possible for a given emitter size to maximize the fluence at the target. From Figure 4, z_0 should be lowered just until the curve touches the upper limit of $w_e = 0.1$, giving the best-case optimization of the laser profile. The optimal focal plane distance was found to be $z_0 = 15.59$ km with a waist radius $w_0 = 0.1$ m. These optimal parameters are used in the laser-debris interaction modelling in later sections.

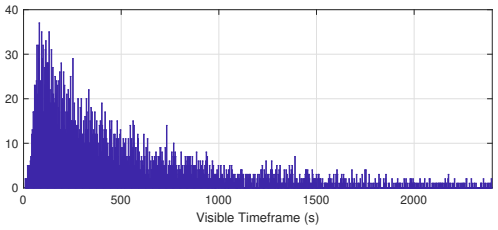

Figure 5. Distribution of visibility window duration

5.6. Impulse Transfer Calculation

5.6.1. Photon Pressure

The database of encounter dynamics obtained in Section 4 is now used to model the interaction of the laser beam with the fragment and obtain a net impulse transfer for each encounter. A total of 7549 viable encounters were extracted from the orbital propagation and used to build this database.

An example of the dynamics extracted from a single encounter can be seen in Figure 4.1, where the orange line is a binary state of observability (all criteria being met) for that instant in time. Thus, only the dynamics during sections where this condition equals 1 are fed into the photon pressure model. The distribution of visibility window duration can be seen in Figure 5.

The separation vectors $\mathbf{S}(t)$ during the observable window for each encounter are passed into the laser-debris interaction (LDI) model described previously. This integrates the laser pressure force over the course of the interaction, accounting for variability in the direction of incidence and magnitude of irradiance over time.

The LDI model outputs a net impulse vector which represents the net momentum transfer of the entire interaction. To facilitate generation of new encounters according to the found distributions, the direction of the impulse is converted from absolute 3D coordinates to a local reference frame for each encounter. The reference frame used sets the origin at the fragment position at the 'centre' of the observability window - where each timestep is weighted by its distance from the satellite. A local instantaneous reference frame is defined which allows the net impulse direction to be expressed in terms of its magnitude, declination and right ascension relative to the negative velocity direction.

Building this large database allows encounters to be 'generated' by selecting random encounters from the database, and applying an impulsive ΔV to different fragment states in its own local reference frame. Using this method ensures that any complex correlations between the dynamics of the encounter and the resultant net impulse are preserved, while still being fast to compute by not requiring the LDI model to be used for every encounter.

5.6.2. Ablation

A similar database is built for the ablative case using the relevant model, with the key difference being the instant at which the impulse is applied. Here, the instant of interaction is chosen randomly. This is because the time to acquire the fragment form the start of the window is not known at this stage. It may be possible to estimate the range to the fragment on the fly and better time the pulse, but this capability is also not assumed in these calculations.

6. LONG TERM MISSION IMPACT MODELLING

Using the results of all previous sections, we are now able to assess the long-term impact of a constellation of satellties deployed into a debris shell as a response to a breakup event.

To achieve this, a new set of 5000 fragments is generated in the same way as before, centered around the same 1200 km altitude.

Interaction times are generated using the same distribution of consecutive event separations found earlier in the representative population, until a full 10-year mission duration's worth of encounters has been generated for a single satellite. For each interaction, a random fragment identifier number is assigned, which is the fragment that is encountered in that instance.

This is repeated for each satellite in the constellation - 100 in the base case - and all events together with their timestamps, fragment identifiers and satellite identifiers are collated into a single database. Exactly half of these events are then randomly selected and removed, to account eclipse conditions where the Sun does not illuminate the fragment, rendering it invisible to the camera. Finally, for consecutive events involving the same spacecraft where the time separation is insufficient to recharge the batteries using solar power are removed leaving only the first of such a consecutive series.

For the remaining encounters, impulsive interactions - magnitude and relative direction - are selected at random from the database built in Section 5.6. This preserves any complex correlations between encounter parameters. This leaves us with a series of interactions for every fragment in the shell.

Fragments' orbits are then individually propagated from $t = 0$ to each subsequent interaction time, where an impulsive ΔV is applied to its state vector before it is propagated to the next encounter. After the final encounter has been reached, the fragment's orbit is then propagated to the end of the 10 year mission span unperturbed. The original orbit is also propagated unperturbed for the full 10 year duration to identify changes due to the applied interactions. During these propagations, for the sake of computation time, the only perturbation in the orbit propagation is atmospheric drag - J2 and other perturbations are disabled.

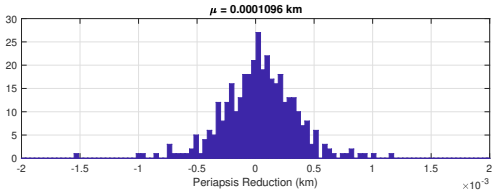

Figure 6. Net change in periapsis (photon pressure)

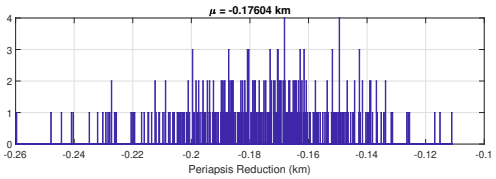

Figure 7. Net change in periapsis (ablation)

6.1. Results

Figures 6 and 8 show the distribution of periapsis change, as well as achieved ΔV for individual interactions and cumulative ΔV for each fragment. In these preliminary results, only 369 of 5000 fragments have been propagated to the end of the 10 year mission duration. As can be seen, the net velocity change is on the order of tens of millimetres per second, and the change in periapsis is negligible, with some fragments even having had their periapsis raised slightly.

Figures 6 to 10 show the same results for the ablation case, as well as the achieved lifetime reduction.

7. DISCUSSION AND CONCLUSION

In this paper, detailed modelling of a concept that could be realistically deployed with current technology was performed to determine the feasibility of reducing the lifetime of a large population of small debris fragments.

The results of these analyses indicate firstly that photon pressure is not a viable mechanism by which to attempt orbit lowering of debris using a space-based platform. The achieved reduction in periapsis was less than a standard deviation from zero, and so the effect was negligible even for a 100-satellite constellation carrying 10kW CW lasers. This mechanism is better suited to collision avoidance, as the achieved ΔV of on the order of mms^{-1}, while not sufficient to lower the orbit, given time could compound enough to avoid a collision. Such approaches however would likely be deployed from ground as prior knowledge of the orbit is a pre-requisite

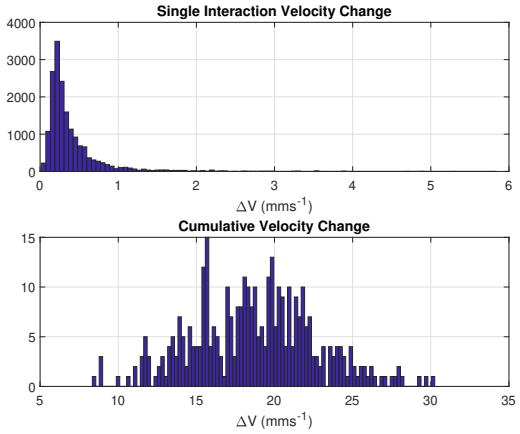

Figure 8. Achieved individual and cumulative (single fragment) ΔV (photon pressure)

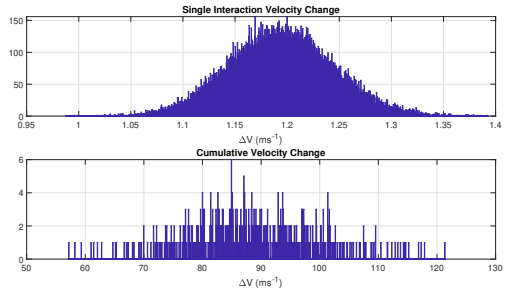

Figure 9. Achieved individual and cumulative (single fragment) ΔV (ablation)

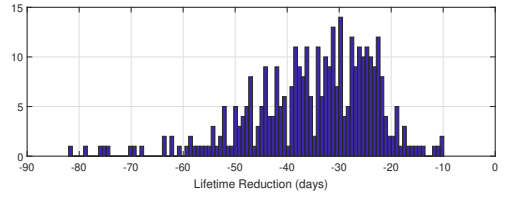

Figure 10. Lifetime reduction (ablation)

Ablation-based interaction, as expected, produced a stronger effect on the orbit, with measurable, but still small, periapsis and lifetime reduction. However, the concept in its current form still likely produces too weak an effect to be feasible. Due to the small size of the effect, it is likely, as noted in Section 5.4, that complete vapourization of small targets would occur before the orbit was substantially lowered beyond the point demonstrated in this paper even if optimizations to the coupling could be achieved. Thus from these results we conclude that orbit-lowering by space-based laser interaction is not feasible, but recommend future work focus on the complete vaporization of such targets

The analyses did show however that previously untracked fragments could be optically acquired by small cameras in orbit. This opens the possibility of a similar concept where the goal could be simply to detect and determine orbits of previously untracked fragments, to better inform collision avoidance strategies.

REFERENCES

1. Amoruso, S. et.al. (2007). *Applied Physics A*, **89**, 1017-1024, Springer
2. Oliver, G. et.al. (2010). *IEEE Transactions on Nuclear Science*, **57**(3), 1644-1653, IEEE
3. Pardini C., Anselmo L. (2011).*Advances in Space Research*, **48**, 557-569, Elsevier
4. Phipps, C. et.al. (2006). *Applied Surface Science*, **252**(13), 4838-4844, Elsevier B.V.
5. Phipps C. R. (2014).*Acta Astronautica*, **104**, 243-255, Elsevier
6. Phipps, C. et.al. (2017). *Journal of Applied Physics*, **122**, 193103, AIP Publishing
7. Shen, S., Xing, J., Chang, H. (2014) *Chinese Journal of Astronautics*, **27** (4), 805-811, CSAA
8. Tran, D. et. al. (2017). *Journal of Applied Physics*, **122**, 233304, AIP Publishing
9. Van, T. A. et. al. (2019) *Optical Engineering*, **58** (8), 086111, SPIE
10. Wang, T. (2010). *Science and Global Security*, **18**(2), 87-118, Taylor and Francis Group
11. Wang, B. (2017). *Applied Physics Letters*, **110**, 014101, AIP Publishing
12. Yang Yang, F. et. al. (2016) *Acta Astronautica*, **126**, 411,423, Elsevier
13. Nobody B., Somebody G., Who D., et al., (1997). *The book*, Publisher, ed. 2
14. Smith A., Jones B., (1996). The new discovery, *Other Journal*, **223**(1), 1029–1101